have a much smaller size than the cooling images at the same temperatures below T_{K1}. This difference may be due to the way in which the sample is cooled. The tip of the MFM vibrates above the sample surface at the lever's resonant frequency of 110 KHz, contacting the sample at the lowest point of each oscillation. At this contact point, the magnetic field applied by the tip is large (10^2 to 10^3 G) (*21*). Roughly, as the tip is scanned, a strong periodic magnetic pulse with a frequency of 110 KHz is scanned over the sample. We believe that upon cooling, although this scanning high-frequency localized magnetic pulse may not change the relative FM fraction (*22*), it can partially align the magnetization of the domains and drive the motion of the domain walls, leading to the merging and enlargement of the domains. On the other hand, the warming images were obtained after the sample was cooled to the lowest temperature in a magnetic field of 25 G. During this cooling process, the tip is far away from the sample. This cooling field may not be strong enough to move the domain walls. When scanning during warming, the domain walls are strongly pinned. As a result, the shape of the domains is unchanged. As T_{P2} is approached, the average magnetization decreases, which results in a rise in the resistivity (Fig. 1B) (*23*). Our observations indicate that during cooling, the percolation of the FM domains causes the steep resistivity drop, whereas during warming, the FM conductive paths remain until near T_{P2}, but the decrease in the average magnetization leads to the jump in resistivity. This also may explain why the knee in the resistivity is sharper during cooling than during warming.

Below T_{K1} the enlargement of the domains is mainly due to the merging of the domains, and not to the increase of the FM volume fraction. Therefore, the resistivity changes slowly below T_{K1}, as shown in Fig. 1B.

Even well above T_{P2}, there is still a slight but discernable contrast in some areas, which can be more clearly seen in the supplemental movies. We propose that this is due to the magnetic inhomogeneity above T_P that is frequently observed in similar CMR materials (*24–26*).

Owing to the constraining effect of the substrate, some effects observed in bulk samples may be suppressed or different for these thin films (*17*). This might account for the sharper transitions in the thin films and the narrower hysteresis regions. This implies that the temperature-dependent magnetic microstructure in thin films may be modified due to the effect of the substrate.

References and Notes

1. R. von Helmot, J. Wecker, B. Hopzapfel, L. Schulz, K. Samwer, *Phys. Rev. Lett.* **71**, 2331 (1993).
2. S. Jin *et al.*, *Science* **264**, 413 (1994).
3. C. Zener, *Phys. Rev.* **82**, 403 (1951).
4. A. J. Millis, *Nature* **392**, 147 (1998).
5. R. Maezono, S. Ishihara, N. Nagaosa, *Phys. Rev. B* **58**, 11583 (1998).
6. A. Asamitsu, Y. Moritomo, Y. Tomioka, T. Arima, Y. Tokura, *Nature* **373**, 407 (1995).
7. C. Martin *et al.*, *Eur. Phys. J. B* **16**, 469 (2000).
8. M. Uehara, S. Mori, C. H. Chen, S. W. Cheong, *Nature* **399**, 560 (1999).
9. M. B. Salamon, M. Jaime, *Rev. Mod. Phys.* **73**, 583 (2001).
10. N. D. Mathur, P. B. Littlewood, *Solid State Commun.* **119**, 271 (2001).
11. C. W. Yuan, E. Batalla, A. de Lozanne, M. Kirk, M. Tortonese, *Appl. Phys. Lett.* **65**, 1308 (1994).
12. Q. Lu, C. Chen, A. de Lozanne, *Science* **276**, 2006 (1997).
13. Materials and methods are available as supporting material on *Science* Online.
14. Park Scientific Instruments (now Veeco Instruments), Santa Barbara, CA.
15. R. Desfeux, S. Bailleul, A. Da Costa, W. Prellier, A. M. Haghiri-Gosnet, *Appl. Phys. Lett.* **78**, 3681 (2001).
16. We recorded another set of cooling and warming images using a temperature change rate of 0.3 K/min. The temperature-dependent evolution of the FM domains is qualitatively the same as that of the sets shown in the text. We believe that our observation is largely due to the temperature change and not time relaxation.
17. V. Podzorov, B. G. Kim, V. Kiryukhin, M. E. Gershenson, S.-W. Cheong, *Phys. Rev. B* **64**, 140406 (2001).
18. A. Biswas *et al.*, *Phys. Rev. B* **61**, 9665 (2000).
19. We emphasize that all of our sets of cooling and warming images obtained on different areas of the sample with different noncontact piezolevers show the same temperature-dependent evolution of domains. As described in the text, during cooling from room temperature to T_{P1}, all the images are uniform, and from low temperature to T_{K2} during warming, both the size and the contrast of the images are nearly unchanged. To maintain the consistency between the resistivity hysteresis and the micromagnetic hysteresis, we have simply reproduced the three highest temperature images in Fig. 1A and the three lowest temperature images in Fig. 1C.
20. P. Levy *et al.*, *Phys. Rev. B* **65**, 140401 (2002).
21. L. Kong, S. Y. Chou, *Appl. Phys. Lett.* **70**, 2043 (1997).
22. F. Parisi, P. Levy, L. Ghivelder, G. Polla, D. Vega, *Phys. Rev. B* **63**, 144419 (2001).
23. A. Urushibara *et al.*, *Phys. Rev. B* **51**, 14103 (1995).
24. Y.-A. Soh, G. Aeppli, N. D. Mathur, M. G. Blamire, *Phys. Rev. B* **63**, 020402 (2000).
25. ———, *J. Appl. Phys.* **87**, 6743 (2000).
26. M. Fäth *et al.*, *Science* **285**, 1540 (1999).

27. The work at Austin was supported by NSF grant DMA-0072834 and The Texas Center for Superconductivity at the University of Houston. The work at Maryland was supported in part by NSF grant MRSEC-00-80008. We thank S.-W. Cheong, N. D. Mathur, A. Guha, Q. Niu, Y. Tsui, and J. Lee for fruitful discussions and T. Ruiter (Veeco Metrology Group) for providing piezoresistive cantilevers.

Supporting Online Material

www.sciencemag.org/cgi/content/full/1077346/DC1
Materials and Methods
Movies S1 to S4

14 August 2002; accepted 9 September 2002
Published online 19 September 2002;
10.1126/science.1077346
Include this information when citing this paper.

Ideal Pure Shear Strength of Aluminum and Copper

Shigenobu Ogata,[1,2,3] Ju Li,[1,4] Sidney Yip[1]*

Although aluminum has a smaller modulus in $\{111\}\langle 11\bar{2}\rangle$ shear than that of copper, we find by first-principles calculation that its ideal shear strength is larger because of a more extended deformation range before softening. This fundamental behavior, along with an abnormally high intrinsic stacking fault energy and a different orientation dependence on pressure hardening, are traced to the directional nature of its bonding. By a comparative analysis of ion relaxations and valence charge redistributions in aluminum and copper, we arrive at contrasting descriptions of bonding characteristics in these two metals that can explain their relative strength and deformation behavior.

The minimum shear stress necessary to cause permanent deformation in a material without imperfections is fundamental to our concept of materials strength and its theoretical limits under large strains (*1*, *2*). With the possible exception of recent nanoindentation measurements (*3*), it has not been feasible to directly measure the ideal shear strength of crystals. The demonstration that this property can be reliably determined by first-principles calculations therefore would have important implications for the understanding of the behavior of solids at the limit of structural stability. Results on stress-strain behavior of Al and Cu in $\{111\}\langle 11\bar{2}\rangle$ shear, calculated with density functional theory (DFT) and accounting for full atomic relaxation, have been reported (*4*), where Cu was found to have a higher ideal shear strength than that of Al. Using various DFT methods and systematically cross-checking the results, we further investigated the shear strength and deformation of Al and Cu and found instead that Al has the higher strength. Here, we report and substantiate our findings by detailing the energetics of shear deformation, the pressure-hardening behavior, and valence charge redistribution during deformation. These considerations show that the ideal shear strength and related

[1]Department of Nuclear Engineering, Massachusetts Institute of Technology, Cambridge, MA 02139, USA. [2]Department of Mechanical Engineering and Systems, [3]Handai Frontier Research Center, Osaka University, Osaka 565–0871, Japan. [4]Department of Materials Science and Engineering, Ohio State University, Columbus, OH 43210, USA.

*To whom correspondence should be addressed. E-mail: syip@mit.edu

properties such as stacking fault energies of Al and Cu can be accurately calculated and that the results can be rationalized by the underlying electronic structure. We suggest that bonding in Al is much more like a "hinged rod," and we emphasize the importance of the breaking and reformation of directional bonds as compared to the isotropic "sphere-in-glue"–like behavior in Cu.

The intrinsic stacking fault energy, a measure of the energy penalty when two adjacent atomic planes in a crystal lattice are sheared relative to each other, is known to play an important role in the structure and energetics of dislocations formed by slip processes. Although it is known experimentally that the intrinsic stacking fault energy is much larger in Al than in Cu, this finding has not been related to their ideal shear strengths. For this purpose, we introduce a general function (Fig. 1A)

$$\gamma_n(x) \equiv \frac{E_n(x)}{nS_0},\ n = 1, 2, \ldots \qquad (1)$$

where x is the relative displacement in the slip direction between two adjacent atomic planes (we focus on $\{111\}\langle 11\bar{2}\rangle$ slip here), $E_n(x)$ is the increase in total energy relative to its value at $x = 0$, with $n + 1$ being the number of planes involved in the shearing and S_0 being the cross-sectional area at $x = 0$. The series of functions $\gamma_1(x)$, $\gamma_2(x)$, . . ., $\gamma_\infty(x)$ may be called the multiplane generalized stacking fault energy, with $\gamma_1(x)$ being the conventional generalized stacking fault energy (GSF) (*5*) and $\gamma_\infty(x)$ being the affine strain energy. The intrinsic stacking fault energy γ_{sf} is $\gamma_1(b_p)$, where $\vec{b}_p = [11\bar{2}]a_0/6$ is the partial Burgers vector (a_0, equilibrium lattice constant). The unstable stacking energy γ_{us}, an important parameter in determining the ductility of the material (*6*), is $\gamma_1(x_0)$, where $d\gamma_1/dx(x_0 < b_p) = 0$. It is instructive to compare different $\gamma_n(x)$ of the same slip system as n varies. The difference should be relatively small from a local "glue" (shaded region in Fig. 1A) viewpoint where we take the valence electron cloud to be the glue. We also have the asymptotic behavior at large n

$$\gamma_n(x) = \gamma_\infty(x) + \frac{2\gamma_{twin}(x)}{n} + \mathcal{O}(n^{-2}) \qquad (2)$$

where $\gamma_{twin}(b_p)$ is the unrelaxed twin boundary energy. The rate of convergence to Eq. 2 reflects the localization range of metallic bonding in a highly deformed bulk environment.

The DFT calculations, following the same procedure previously described (*4*), were performed with our own plane wave code and four other packages, Vienna ab Initio Simulation Package (VASP) (*7*, *8*), Cambridge Serial Total Energy Package (CASTEP) (*9*), WIEN2k (*10*), and ABINIT (*11*), with different setups used to cross-check each other. The results reported here are primarily those obtained from VASP with Perdew-Wang (PW91) generalized gradient approximation (GGA) exchange-correlation density functional (*12*), ultrasoft (US) pseudopotential (*8*), and Methfessel-Paxton smearing method (*13*) with 0.3-eV smearing width, and the cell being oriented as in Fig. 1A. The cutoff energies for the plane wave basis set for Al and Cu are 162 and 292 eV, respectively. Table 1 shows the agreement of our results with experimental and other calculations. To compute the equilibrium lattice constant a_0, as well as relaxed and unrelaxed $\{111\}\langle 11\bar{2}\rangle$ shear moduli (G_r' and G_u', respectively) (*4*), we use a six-atom supercell of three $\{111\}$ layers. After relaxation, all stress components

Table 1. Benchmark results, comparison of present calculations (Calc), experiments (Expt), and previous calculations (Oth calc). Dashes indicate that results are not available.

Variable	Al			Cu		
	Calc*	Expt	Oth calc	Calc*	Expt	Oth calc
a_0 (Å)	4.04	4.03†	4.04‡	3.64	3.62†	3.64§
G_r' (GPa)	25.4	27.4‖	19–25¶	31.0	33.3‖	26–34¶
G_u' (GPa)	25.4	27.6‖	24–30¶	40.9	44.4‖	36–44¶
γ_{sf} (mJ/m^2)	158	166#	143**, 164††	39	45#	(49)‡‡
γ_{us} (mJ/m^2)	175	—	183**, 224††	158	—	(210)‡‡

*VASP, US-GGA, 18 × 25 × 11 Monkhorst-Pack $\vec{k}$ points. †(*25*) Al at temperature $T = 0$ K, Cu at $T = 298$ K. ‡(*26*) GGA. §(*27*) Full-potential linearized augmented plane wave method (WIEN97 program), GGA. ‖(*28*) calculated from elastic constants at $T = 0$ K. ¶(*4*) LDA. #(*29*). **(*30*) LDA. ††(*31*) LDA. ‡‡(*5*) LDA, unrelaxed.

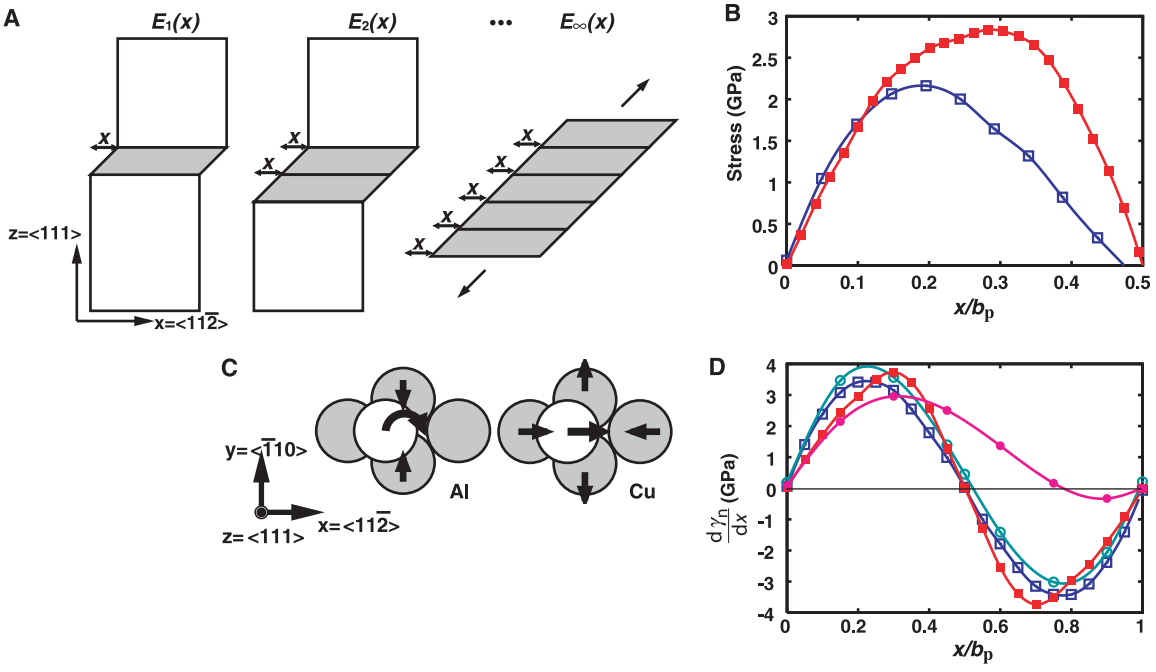

Fig. 1. (**A**) Multiplane generalized stacking fault energy: $n = 1, 2, \ldots, \infty$. (**B**) Pure shear stress–displacement responses of Al (solid squares) and Cu (open squares) and (**C**) ion relaxation patterns in Al and Cu. (**D**) Simple shear stress–displacement curves $d\gamma_\infty(x)/dx$ (squares) compared to $d\gamma_1(x)/dx$ (circles) in Al (solid symbols) and Cu (open symbols).

other than σ_{13} ($=\sigma_{31}$) are reduced to <0.1 GPa. For the intrinsic and unstable stacking energies γ_{sf} and γ_{us}, respectively, we use a 24-atom supercell of 12 layers for Al (10 layers for Cu) with layers 1 and 12 facing vacuum and shearing between layers 6 and 7. Relaxation of all layers along the <111> direction is terminated when the force on each atom is <0.01 eV/Å. Al has a much larger γ_{sf} value than that of Cu, yet their γ_{us} values are quite close.

For affine deformation calculations, we consider pure shear ($\sigma_{ij} = 0$, except σ_{13}) and simple shear ($x \neq 0$ with no relaxations). The corresponding stress-displacement curves are shown in Fig. 1, B and D, respectively. The stress values are obtained from analytical expressions; they have been checked against numerical energy derivatives at several values of strain. After analyzing the effects of smearing width, energy cutoff, and Brillouin zone integration $\vec{k}$-point convergence, we estimate that the maximum stress values in Table 2 have an uncertainty of <0.1 GPa within each method used. ABINIT uses the Perdew-Burke-Ernzerhof GGA functional (*14*) and norm-conserving Troullier-Martins (TM) pseudopotential (*15*); CASTEP uses PW91-GGA/US; our own plane wave code uses PW91-GGA/TM; and WIEN2k is a full-potential augmented plane wave plus local orbitals method, where the core and valence states are treated by the Dirac equation and the scalar-relativistic approximation, respectively (*10*). Furthermore, the full-potential projector augmented-wave (PAW) method (*16*) and the local density approximation (LDA) options of VASP also have been included in the cross-check. The difference between US and PAW is <5% in the maximum stress values, and LDA consistently gives a stress that is 10 to 20% higher than that of GGA. With all methods used, Al is found to have ideal simple shear and pure shear strengths that are higher than those of Cu (Table 2) (*17*).

At equilibrium, Cu is considerably stiffer than Al; its bulk, simple, and pure shear (along $\{111\}\langle 11\bar{2}\rangle$) moduli are greater than those of Al by 80, 65, and 25%, respectively. However, Al has an ideal pure shear strength that is 32% larger than that of Cu because it has a longer range of elastic strain before softening (Fig. 1B): $x_{max}/b_p = 0.28$ or $\gamma_{max} = 0.20$ in Al, which are the displacement and the engineering shear strain at the maximum shear stress, respectively, versus $x_{max}/b_p = 0.19$ or $\gamma_{max} = 0.13$ in Cu. The ion relaxations in these two metals are different (Fig. 1C). In Al, when the top atom slides over the bottom atoms, the top atom hops in the *z* direction, and the bottom atoms contract in the *y* direction (relaxation in *x* is almost zero). In Cu, there is almost no relaxation in the *z* direction; the top atom translates essentially horizontally, and the bottom atoms expand and contract in the *y* and *x* directions, respectively.

The difference in relaxation patterns has important implications for the shear strength–hardening behavior (Table 3), which also has been noted and discussed in terms of third-order elastic constant (*18*). When pressurized in the ⟨110⟩ direction, Cu hardens, whereas Al softens substantially; however, if pressurized in the ⟨111⟩ direction, Al hardens substantially, whereas Cu softens slightly. These results show that the pressure-hardening effect is highly dependent on orientation. A rough estimate of the stress state at the displacement burst observed in nanoindentation experiments (*3*) shows that the pressure components are at the level indicated in Table 3. Thus, a large effect on the shear strength is to be expected. However, because the actual stress state is a complicated triaxial condition and given that the pressure-hardening behavior is very anisotropic, one cannot ascertain its real effect without an accurate stress analysis. For this purpose, we apply a method combining atomistic and finite-element calculations (*19*).

Because Al has no core d states, its partially occupied valence d bands are abnormally low in energy, which gives rise to directional bonding. At the six-atom interstice in Al, the pocket of charge density has cubic symmetry and is very angular in shape, with a volume comparable to the pocket centered on every ion (Fig. 2A). In Cu, there is no such

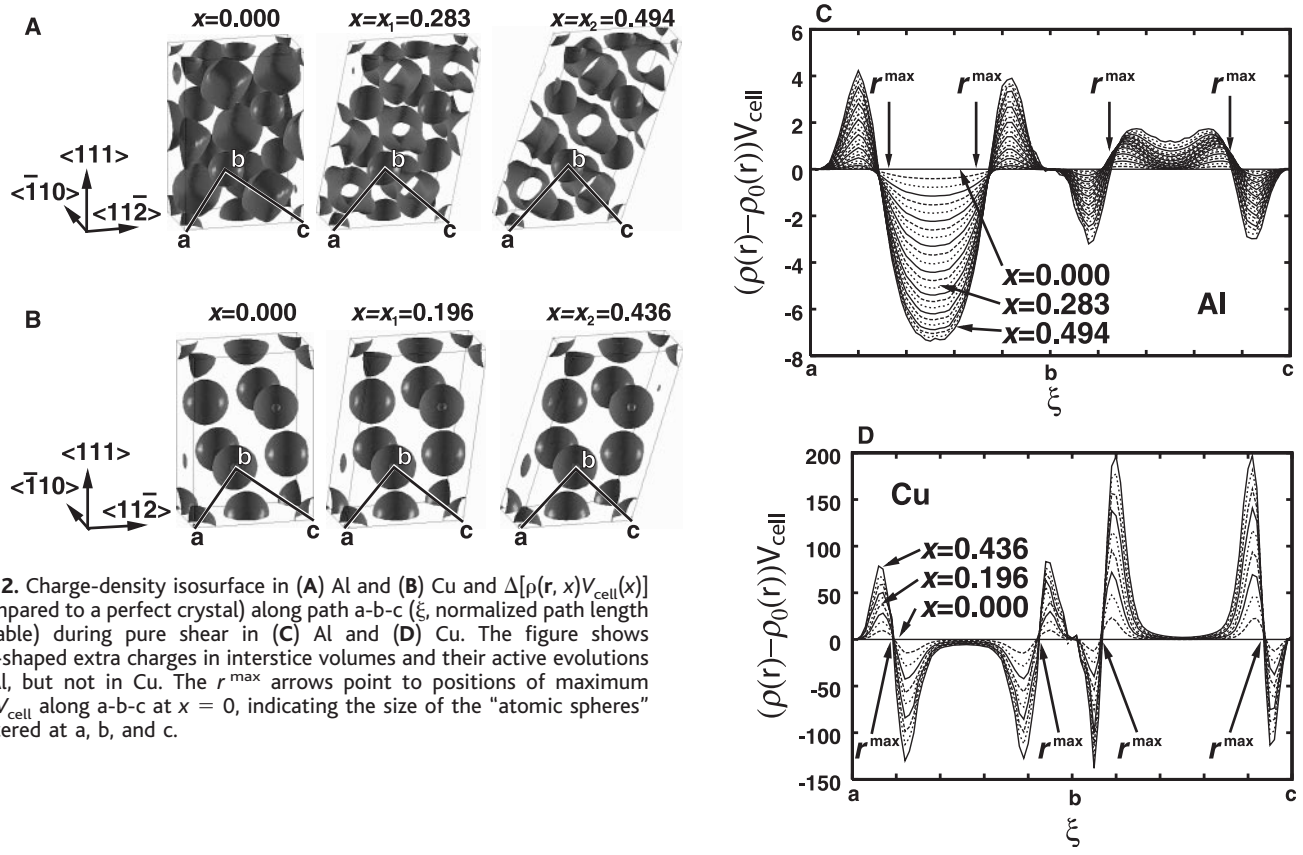

Fig. 2. Charge-density isosurface in (**A**) Al and (**B**) Cu and $\Delta[\rho(\mathbf{r}, x)V_{cell}(x)]$ (compared to a perfect crystal) along path a-b-c (ξ, normalized path length variable) during pure shear in (**C**) Al and (**D**) Cu. The figure shows box-shaped extra charges in interstice volumes and their active evolutions in Al, but not in Cu. The r^{max} arrows point to positions of maximum $\rho(\mathbf{r})V_{cell}$ along a-b-c at $x = 0$, indicating the size of the "atomic spheres" centered at a, b, and c.

Table 2. Ideal simple shear and pure shear strengths (σ^u and σ^r, respectively).

Code (number of $\vec{k}$ points)	Al		Cu	
	σ^u (GPa)	σ^r (GPa)	σ^u (GPa)	σ^r (GPa)
VASP (12 × 17 × 7)	3.67*	2.76*	3.42	2.16
VASP (18 × 25 × 11)	3.73	2.84	3.44†	2.15†
VASP (21 × 28 × 12)	—	—	3.45†	2.15†
VASP (27 × 38 × 16)	3.71*	2.84*	—	—
CASTEP (13 × 22 × 9)	—	—	3.22†	2.10†
CASTEP (17 × 29 × 12)	3.73*	2.84*	—	—
WIEN2k (38 × 33 × 38)‡	3.83*	2.98*	3.61†	2.23†
ABINIT (12 × 17 × 7)	3.68*	2.84§	—	—
ABINIT (18 × 25 × 11)	3.71*	2.90*	—	—
Own code (12 × 17 × 7)	3.73*	2.89*	3.48†	2.18†

*Cell dimension from VASP (18 × 25 × 11) calculations. †Cell dimension from VASP (12 × 17 × 7) calculations. ‡ One-atom cell (atomic sphere radius R_{mt} = 2.2 bohr; plane wave cutoff $K_{max}R_{mt}$ = 10; charge density Fourier expansion cutoff G_{max} = 20 ryderg$^{1/2}$). §Cell volume was relaxed by using ABINIT.

Table 3. Maximum shear stress under external loading. P, hydrostatic pressure; σ_{yy} and σ_{zz}, normal stress in the *y* and *z* directions, respectively.

External stress	Al (GPa)	Cu (GPa)
$P = 0$ (GPa)	2.84	2.16
$P = 10$ (GPa)	4.49	2.46
$P = 20$ (GPa)	5.90	2.84
$\sigma_{yy} = -10$ (GPa)	1.78	3.12
$\sigma_{yy} = -20$ (GPa)	1.41	3.54
$\sigma_{zz} = -3$ (GPa)	3.64	2.03
$\sigma_{zz} = \sigma_{yy} = -10$ (GPa)	3.98	4.38
$\sigma_{zz} = \sigma_{yy} = -20$ (GPa)	5.26	6.52

interstice pocket, and the charge density is nearly spherical about each ion (Fig. 2B). Thus, Al has an inhomogeneous charge distribution in the interstitial region because of bond covalency (*20*) and directional bonding (*21*), whereas Cu has relatively homogeneous distribution and little bond directionality. To probe these bonding characteristics further, we look at how the valence charge density $\rho(\mathbf{r}, x)V_{cell}(x)$ varies along a path in cell, a-b-c, during pure shear, as atom b moves away from its initial nearest neighbor atom a (at $x = x_1$) and takes on a new nearest neighbor atom c (at $x = x_2$). The $\Delta[\rho(\mathbf{r}, x)V_{cell}(x)]$ patterns, with V_{cell} being the cell volume, for Al and Cu again show substantial contrast. In Al (Fig. 2C), the maximum change occurs halfway between the two nearest ions, which indicates that when atoms change neighbors, the breaking and reformation of directional bonding is an important activity. There is little such activity in Cu (Fig. 2D). $\Delta[\rho(\mathbf{r}, x)V_{cell}(x)]$ mainly reflects an accommodation process, like soft spheres squeezing past each other by distorting their own shape. A similar attempt to connect stacking fault energy with redistribution and topological properties of charge density was made recently (*22*).

The charge-density behavior just discussed, along with the relaxation patterns seen in Fig. 1C, suggest a hinged-rod model to describe the shear strength for Al, in contrast to the conventional "muffin-tin" or sphere-in-glue model for Cu. It is reasonable to think that when the bonding is directional (rodlike), a longer range of deformation can be sustained before breaking than when the bonding is spherically symmetric, because of different geometrical factors of charge-density decay with bond length. In covalent systems like Si (*23*) and SiC, we verified that during shear, the bonds generally do not break until the engineering shear strain reaches 25 to 35%, which is substantially larger than those of metallic systems. Conversely, when the bonds do break, a directionally bonded system can be expected to be more frustrated and less accommodating, as manifested in a larger intrinsic stacking fault energy, for example.

To quantify our interpretation, we return to the behavior of the multiplane generalized stacking fault energies in the form of stress-displacement functions $d\gamma_1(x)/dx$ and $d\gamma_\infty(x)/dx$ (Fig. 1D). First, we note that for Cu, $d\gamma_1(x)/dx$ and $d\gamma_\infty(x)/dx$ are not very different across the entire range of shear, so the local glue picture is appropriate. The fact that the sliding of a layer is effectively decoupled from that of adjacent layers indicates that bonding in Cu has nearly no bond-angle dependence. On the other hand, the same functions behave much more differently in Al, especially when $x > x_{max}$, at which the gradient reaches a maximum. Even in the range of $x < x_{max}$, the relative magnitudes of $d\gamma_1(x)/dx$ and $d\gamma_\infty(x)/dx$ are opposite in order in Al as compared to those in Cu, suggesting a possibly different nature of bonding. Second, the value of x_{max} is almost identical between $d\gamma_1(x)/dx$ and $d\gamma_\infty(x)/dx$ in both Al and Cu, with Al having the larger x_{max} value, implying that the longer range directional bonding in Al could be a more general feature than being specific to the affine strain energy $\gamma_\infty(x)$. Third, we see that when $x \gg x_{max}$ and the directional bonds in Al are broken (confirmed by a depleted charge at the interstice in Fig. 2C), $d\gamma_1(x)/dx$ in Al stays positive for an extended range, whereas $d\gamma_1(x)/dx$ in Cu becomes negative quickly. Thus, although Al and Cu have approximately the same unstable stacking energy (Table 1), we see that when the displacement *x* reaches b_p and the configuration becomes an intrinsic stacking fault, Cu has recovered most of its losses in the sense of a low value of γ_{sf}, whereas Al has recovered very little as its γ_{sf} value remains close to the γ_{us} value. The implication is that when a directional bond is broken, it is more difficult for the electrons to readapt. In contrast, for sphere-in-glue–type systems, even if the bond angles are wrong, as long as the volumes fit as in the intrinsic stacking fault, the electrons can redistribute well, and the system does not incur a large energy penalty.

In this work, we exploit the connection between the generalized stacking fault energy and the stress-strain response to show that the abnormally high ideal shear strength and intrinsic stacking fault energy of Al have the same electronic-structure origin (namely, directional bonding). On one hand, directional bonds give rise to a relatively longer shear deformation range, which accounts for the larger ideal shear strength of Al in relation to that of Cu; on the other hand, once the existing bonds are broken and new bonds are formed with unfavorable bond angles, the electrons cannot readjust easily, resulting in an anomalous intrinsic stacking fault energy for Al. Our findings are supported by the detailed behavior of the valence charge density obtained from first-principles calculations that have been systematically cross-checked. We studied the pressure dependence of the shear strength and have shown its very anisotropic character. These results suggest that conventional crystal plasticity notions such as a scalar or pressure-independent yield criterion based on critical resolved shear stress, although successful for macroscopic face-centered cubic metals, should be viewed cautiously when interpreting nanoindentation experiments (*3*). Contemporary empirical potentials (*24*) may be useful for providing a qualitative description of the nonlinear, anisotropic stress distribution under the nanoindenter and for ascertaining the likely site and character of the instability; the quantitative importance of these results remains to be scrutinized by more accurate ab initio calculations.

References and Notes

1. J. Wang, J. Li, S. Yip, S. Phillpot, D. Wolf, *Phys. Rev. B* **52**, 12627 (1995).
2. J. W. Morris Jr., C. R. Krenn, *Philos. Mag. A* **80**, 2827 (2000).
3. A. Gouldstone, H. J. Koh, K. Y. Zeng, A. E. Giannakopoulos, S. Suresh, *Acta Mater.* **48**, 2277 (2000).
4. D. Roundy, C. R. Krenn, M. L. Cohen, J. W. Morris, *Phys. Rev. Lett.* **82**, 2713 (1999).
5. J. A. Zimmerman, H. Gao, F. F. Abraham, *Model. Simul. Mater. Sci. Eng.* **8**, 103 (2000).
6. J. R. Rice, G. E. Beltz, *J. Mech. Phys. Solids* **42**, 333 (1994).
7. G. Kresse, J. Hafner, *Phys. Rev. B* **47**, RC558 (1993).

8. G. Kresse, J. Furthmüller, *Phys. Rev. B* **54**, 11169 (1996).
9. V. Milman *et al.*, *Int. J. Quantum Chem.* **77**, 895 (2000).
10. P. Blaha, K. Schwarz, G. Madsen, D. Kvasnicka, J. Luitz, *WIEN2k, An Augmented Plane Wave + Local Orbitals Program for Calculating Crystal Properties* (Technische Universität Wien, Vienna, 2001).
11. The ABINIT code is a common project of the Université Catholique de Louvain (Louvain-la-Neuve, Belgium), Corning Incorporated (Corning, NY), and other contributors (available at www.abinit.org).
12. J. P. Perdew *et al.*, *Phys. Rev. B* **46**, 6671 (1992).
13. M. Methfessel, A. T. Paxton, *Phys. Rev. B* **40**, 3616 (1989).
14. J. P. Perdew, K. Burke, M. Ernzerhof, *Phys. Rev. Lett.* **77**, 3865 (1996).
15. N. Troullier, J. L. Martins, *Phys. Rev. B* **43**, 1993 (1991).
16. G. Kresse, D. Joubert, *Phys. Rev. B* **59**, 1758 (1999).
17. For verification, the input files for the different codes are maintained at a publicly accessible Web site (available at http://asm.mit.edu/sogata/AlCu/).
18. C. R. Krenn, D. Roundy, J. W. Morris Jr., M. L. Cohen, *Mater. Sci. Eng. A* **317**, 44 (2001).
19. J. Li, K. J. Van Vliet, T. Zhu, S. Yip, S. Suresh, *Nature* **418**, 307 (2002).
20. P. J. Feibelman, *Phys. Rev. Lett.* **65**, 729 (1990).
21. J. C. Grossman, A. Mizel, M. Côté, M. L. Cohen, S. G. Louie, *Phys. Rev. B* **60**, 6343 (1999).
22. N. Kioussis, M. Herbranson, E. Collins, M. E. Eberhart, *Phys. Rev. Lett.* **88**, 125501 (2002).
23. Y. Umeno, T. Kitamura, *Mater. Sci. Eng. B* **88**, 79 (2002).
24. Y. Mishin, M. J. Mehl, D. A. Papaconstantopoulos, A. F. Voter, J. D. Kress, *Phys. Rev. B* **63**, 224106 (2001).
25. Landolt-Börnstein III/14a, *Structure Data of Elements and Intermetallic Phases. Elements, Borides, Carbides, Hybrides*, K.-H. Hellwege, A. M. Hellwege, Eds. (Springer-Verlag, New York, 1988).
26. C. Stampfl, C. G. Van de Walle, *Phys. Rev. B* **59**, 5521 (1999).
27. F. Jona, P. M. Marcus, *Phys. Rev. B* **63**, 094113 (2001).
28. Landolt-Börnstein III/29a, *Low Frequency Properties of Dielectric Crystals Second and Higher Order Elastic Constants*, D. F. Nelson, Ed. (Springer-Verlag, New York, 1992).
29. J. P. Hirth, J. Lothe, *Theory of Dislocations* (Wiley, New York, ed. 2, 1982).
30. J. Hartford, B. von Sydow, G. Wahnström, B. I. Lundqvist, *Phys. Rev. B* **58**, 2487 (1998).
31. G. Lu, N. Kioussis, V. V. Bulatov, E. Kaxiras, *Phys. Rev. B* **62**, 3099 (2000).
32. We thank J. W. Morris Jr. for comments on the manuscript. S.O. thanks Y. Shibutani and H. Kitagawa for discussions and acknowledges support by a Murata-Kaigai-Ryugaku-Syogakukai fellowship. J.L. and S.Y. acknowledge support by Honda R&D; the Air Force Office of Scientific Research; NSFKDI and ITR initiatives; and Lawrence Livermore National Laboratory.

26 July 2002; accepted 11 September 2002

The Effect of Size-Dependent Nanoparticle Energetics on Catalyst Sintering

Charles T. Campbell, Stephen C. Parker, David E. Starr

Calorimetric measurements of metal adsorption energies directly provide the energies of metal atoms in supported metal nanoparticles. As the metal coverage increases, the particles grow, revealing the dependence of this energy on particle size, which is found to be much stronger than predicted with the usual Gibbs-Thompson relation. It is shown that this knowledge is crucial to accurately model long-term sintering rates of metal nanoparticles in catalysts.

Metal nanoclusters, dispersed across the surface of an oxide or other support, can be much more active and selective as catalysts than can larger metal particles (*1*, *2*). However, metal nanoclusters invariably sinter (form larger clusters) under reaction conditions, especially in some very important technical catalysts (*2*–*8*). The development of supported metal nanoclusters that resist long-term sintering has been hampered by the lack of a kinetic model that accurately predicts long-term sintering based on short-term measurements. Without such a model, every promising new catalyst must be tested for the actual length of time it must resist sintering in application (~1 year).

We show here that the inclusion of accurate size dependence of particle energies in kinetic models is crucial in this respect. Little is currently known experimentally about the energetics of atoms within metal nanoparticles, although the energy of gaseous Sn clusters as a function of size was measured recently (*9*), and theoretical calculations continue to address this important issue (*10*, *11*). The direct determination of particle energies via calorimetry has been developed relatively recently. In addition, the roughness of real catalyst supports can make it difficult to determine particle sizes via microscopic methods as a function of temperature. In the absence of direct measurements, a commonly used approach for estimating the dependence of particle energy on size has been to use the Gibbs-Thompson relation, which states that the chemical potential (partial molar free energy) of a metal atom in a particle of radius R, $\mu(R)$, differs from that in the bulk [$\mu(\infty)$] by

$$\mu(R) - \mu(\infty) = 2\gamma\Omega/R \qquad (1)$$

where γ is the surface free energy of the metal and Ω is the bulk metals volume per atom (*4*, *12*). The use of this relation is implicit in all current atomistic models of sintering (*13*–*15*), starting with the pioneering models of Wynblatt and Gjostein (W-J) (*3*, *4*).

In this report, we use our recent microcalorimetric measurements of the heat of adsorption (q_{ad}) of Pb onto MgO(100) (*16*) to show that the energy of a metal atom in a nanoparticle increases much more dramatically with decreasing size than predicted by the Gibbs-Thompson relation. Because the Pb immediately forms Pb nanoparticles upon adsorption, and these grow in radius smoothly with increasing coverage, this measured adsorption energy versus coverage directly provides the difference in energy between gaseous Pb and a Pb atom in a nanoparticle as a detailed function of particle size (Fig. 1). We then develop a model for predicting particle size evolution based on modified bond additivity that better approximates the calorimetric data. Kinetic models of sintering rates based on our modified bond-additivity estimate are compared to the W-J model, as well as to heuristic models that have been developed because of the inaccuracies of the W-J model. We use our modified bond-additivity model to predict the sintering of gold particles on TiO_2 and compare these model results to experimental data we obtained via temperature-programmed low-energy ion scattering (TP-LEIS).

We can convert our calorimetric data for Pb on MgO(100) (*16*) to energy versus particle size, because there is good evidence that Pb grows on this surface as nearly hemispherical particles with roughly constant number density of $\sim 8.1 \times 10^{11}$ islands/cm^2, after the first few percent of a monolayer. Using this particle density, the measured Pb surface concentration can be converted directly into the average number of atoms per particle, and then into the average hemispherical particle radius (Fig. 1). As can be seen, the stability of the metal atoms in a Pb particle (that is, their heat of adsorption, relative to gaseous Pb) decreases dramatically as the radius decreases below a few nanometers (*17*). For comparison to these direct measurements of the effect of the metal particle size on the metal atom's energy, the predictions of the Gibbs-Thompson relation [Eq. 1, taking $\gamma = 58.6$ μJ/cm^2 for Pb (*18*)] are also plotted in Fig. 1 as "constant γ model". Here, we neglect entropy differences (*12*), so that $q_{ad}(R) - q_{ad}(\infty) = -[\mu(R) - \mu(\infty)] = -2\gamma\Omega/R$, where $q_{ad}(R)$ is the differential molar heat of adsorption of Pb at fixed radius R. As is seen, Eq. 1 severely overpredicts the stability of Pb in small Pb particles, by ~60 kJ/mol at 1 nm radius (*19*). This shows that the surface energy increases substantially as the radius decreases below ~3 nm, which could be ex-

Department of Chemistry, Box 351700, University of Washington, Seattle, WA 98195–1700, USA.